American Mineralogist, Volume 69, pages 252–263, 1984

Stacking disorder in clinochlore chlorite

GERARD E. SPINNLER, PETER G. SELF

Department of Geology
Arizona State University, Tempe, Arizona 85287

SUMIO IIJIMA

Department of Physics
Research and Development Corporation of Japan
Meijo University, Yagoto-Urayama Tepaku-Ku, Nagoya, Japan

AND PETER R. BUSECK

Department of Geology and Department of Chemistry
Arizona State University, Tempe, Arizona 85287

Abstract

We show that HRTEM is useful for distinguishing the one-layer polytypes of chlorite and for characterizing layer stacking sequences. HRTEM images were computed for all one-layer chlorite polytypes. These computations show that the features in HRTEM images can be used to determine the projected shift vectors across the T layers and B sheets. These vectors can, in turn, be used to distinguish among the several possible chlorite polytypes. Five distinct projections result from viewing all possible one-layer chlorite polytypes down their ⟨100⟩ or ⟨110⟩ zone axes (assigning $[\bar{1}00]$ parallel to the talc-stagger direction). Complete specification of polytypes requires either HRTEM combined with X-ray diffraction analysis or HRTEM images from more than one major zone of the same crystal.

A clinochlore sample from West Chester, Pennsylvania, was used as an example of the use of HRTEM to study chlorite polytypism. Single-crystal X-ray analysis showed the sample to be an ordered one-layer IIb-2 polytype. Electron diffraction patterns from a much smaller volume of crystal than was used for the X-ray measurements show streaking parallel to $\mathbf{c}^*$ in the $k \neq 3n$ reciprocal lattice rows, indicating $b/3$ shifts of the chlorite layers.

High-resolution imaging of this crystal illustrates the regular alternation of the T layers and B sheets. In addition, semi-random stacking sequences are the dominant type of disorder whereas layer rotations occur less frequently.

Introduction

The chlorite minerals comprise a large family of rock-forming silicates that consist of alternating talc-like layers (ideally $Mg_3Si_4O_{10}(OH)_2$) and brucite-like sheets (ideally $Mg_3(OH)_6$), hereafter designated "T" and "B," respectively.[1] In chlorites it is possible to have extensive structural disorder resulting from the rotation and shifts of successive layers and from the intercalation of layers of different structure and composition. The first two of these features can give rise to polytypism.

Most observed chlorite polytypes are of the one-layer type and result from the different ways the T layers and B sheets are stacked. Bailey and Brown (1962) used X-ray measurements and geometrical analysis to determine that twelve distinct one-layer polytypes are possible. In addition, semi-random stacking sequences of one-layer polytypes have been recognized from single-crystal X-ray studies.

X-ray diffraction analysis is most successful for identifying the polytype of perfect crystals or identifying individual polytypes in those cases where stacking disorder is limited. However, the majority of chlorites exhibit structural disorder, and for these specimens X-ray methods yield information primarily on the average structure of the crystal. Because of this complexity, structural studies of the chlorites have been limited and relatively few single-crystal X-ray studies have been attempted.

[1] Bailey (1980) suggested that the preferred nomenclature for the structural components of chlorite is 2:1 layer when referring to the talc-like layer and interlayer sheet when referring to the brucite-like sheets. The convention used in this paper facilitates labelling of HRTEM images.

0003–004X/84/0304–0252$02.00

In the present paper, we utilize single-crystal X-ray precession methods, high-resolution transmission electron microscopy (HRTEM), and electron diffraction techniques to study the most common of the chlorite polytypes, chlorite-IIb. This study demonstrates not only the applicability of HRTEM (as suggested by Iijima and Buseck, 1977), but also the limitations of using HRTEM for studying stacking disorder in these minerals.

A large crystal of chlorite from West Chester, Pennsylvania, with a composition corresponding to clinochlore (Table 1), was used for this study. The sample was prepared by ultra-microtomy of epoxy-embedded samples (Iijima and Buseck, 1978). Electron microscopy was performed with a JEOL JEM 100B operated at 100kV. Although the crystals are sensitive to radiation damage, imaging was possible for several minutes at low beam intensity. The on-screen magnification of the images was set at maximum of 100,000×. Crystals were aligned with a goniometer stage so that their [100], [110] or [1$\bar{1}$0] directions were parallel to the incident electron beam. Portions of this same crystal were used also for the X-ray precession measurements.

Polytypism and structure

One-layer chlorite

Bailey and Brown (1962) derived the theoretical one-layer chlorite polytypes, and in this section we briefly review those portions of their work that are relevant to the interpretation of our electron micrographs.

Table 1. Electron microprobe analysis of chlorite from West Chester, Pennsylvania

	Weight percents	Number of ions on the basis of 36 (O, OH)	
SiO_2	30.5	5.82	8.00
TiO_2	0.01		
Al_2O_3	18.7	2.18 2.04	
Cr_2O_3	1.0	.15	
FeO	3.5	.56	12.02
MgO	32.4	9.23	
NiO	0.2	.04	
CaO	n.d.		
Na_2O	n.d.		
K_2O	n.d.		
H_2O^+ (est)	12.5	15.95	
Total	98.8		

(n.d. = not detected, est. = estimated)

Formula:

$(Mg_{9.23}Al_{2.04}Fe^{+2}_{.56}Cr_{.15}Ni_{.04})[(Si_{5.82}Al_{2.18})O_{20}](OH)_{15.95}$

The idealized structure of chlorite is illustrated in Figure 1. A single "chlorite unit" is made up of a T layer plus a B sheet; they are positioned to optimize hydrogen bonding between them. There is a displacement of magnitude $a/3$ between the No. 1 and the No. 4 planes of the T layer. This displacement defines the "talc stagger," which lies in (001) and is parallel to $-\mathbf{a}_1$, as shown in Figure 1b.

One-layer polytypism in chlorite results from (1) the position of octahedral sites in the B sheet relative to an initial T layer, (2) the orientation of the B sheet relative to an initial T layer, and (3) the articulation of the repeating T layer. The two possible sets of octahedral sites in a B sheet are designated I and II. The B sheet can be placed on an initial T layer in two different positions, a and b, thus generating four distinct chlorite units (Ia, Ib, IIa, IIb). The articulation of the repeating T layer completes the description of the chlorite polytypes.

Since one-layer polytypes are being considered, each polytype must be made up of only one of the four chlorite units. Furthermore, the orientation of the repeating T layer (in relation to the talc stagger) has to be the same as the initial T layer, i.e., rotations are precluded. Each of the four possible chlorite units can be stacked in six different arrangements (assuming ideal hexagonal symmetry in each layer) to ensure hydrogen bonding, thus generating 24 polytypes. Twelve of these 24 polytypes are unique and are listed in Table 2.

A displacement vector is defined as extending from the OH in the center of the hexagonal ring in plane No. 2 to the equivalent position in plane No. 8 (Fig. 1) and in most cases coincides with the c-axis. Symmetry and unit cell shape of chlorite determine the orientation of this vector relative to the talc-stagger direction. There are three orientations of this vector corresponding to the three unit cell types of chlorite: (1) If the structure has mirror symmetry and a monoclinic unit cell, the component in (001) of the displacement vector is parallel or antiparallel to the talc-stagger. In these cases the space group is $C2/m$ or Cm. (2) An orthogonal unit cell with mirror symmetry results in a displacement vector perpendicular to (001) and space groups $C2/m$ or Cm. (3) For chlorite units that do not have mirror symmetries ($C1$ or $C\bar{1}$), the component in (001) of the displacement vector is not parallel to the talc stagger.

In each of the above cases, if the projected displacement vector is parallel to one of the three **a**-axes of Figure 1b, the component of the displacement vector in the basal plane is equal to $a/3$, and a monoclinic cell with $\beta = 97°$ results. If the projection of the displacement vector is perpendicular to any of the three **a**-axes, the resultant displacement equals $a/\sqrt{3}$, and a triclinic cell results with $\alpha = 102°$ and $\beta = \gamma = 90°$

Structure projections

The [100], [110], and [1$\bar{1}$0] zone axes, as shown in Figure 2, are useful directions for studying chlorite. For

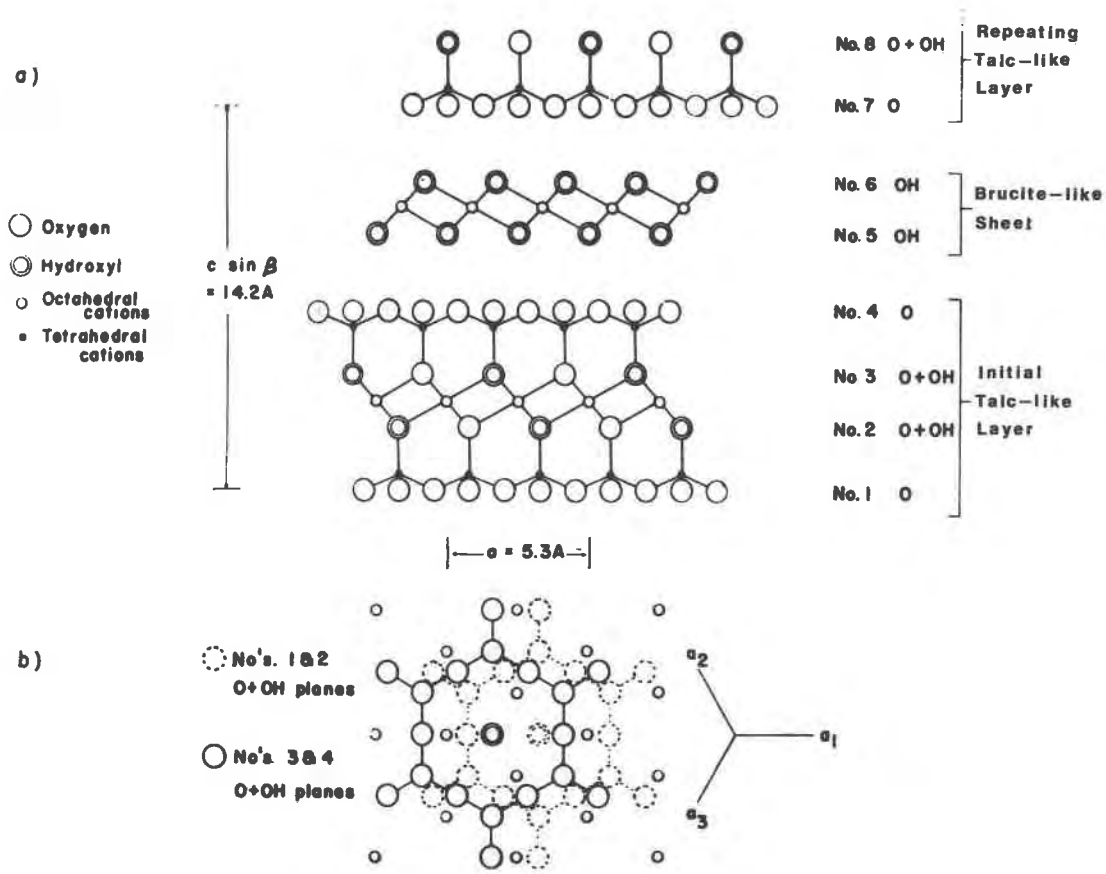

Fig. 1. Idealized chlorite structure (type IIb). (a) (010) projection. The anion planes are numbered to facilitate discussion in the text of possible stacking variations. (b) (001) projection of initial T layer, omitting tetrahedral cations. The axes in Fig. 1b are not necessarily the same for all polytypes. (From Bailey and Brown, 1962).

convenience, we have defined [$\bar{1}$00] parallel to the direction of the *a*/3 talc stagger. When projected along these axes, the 12 distinct one-layer polytypes of chlorite are reduced to five sets of unique projections. Illustrated in Figure 3 are I-beam representations of these projections. Each I-beam is a segment of the T layer (Fig. 4), and its width equals the *b* dimension.

The I-beam representation of layer-silicate structures can be used to illustrate the offsets across the T layers and B sheets, as shown by the dashed vectors (Fig. 3). The displacement across the chlorite unit (TB) is represented by the solid vector, termed the chlorite shift vector. This vector is equivalent to but slightly shifted from that defined by Bailey and Brown (1962).

In projections A and B of Figure 3 there appear to be no offsets across the T layers, as can be seen by the vertical dashed lines; this lack of projected offset is denoted by T_0. An offset between the No. 1 and No. 4 planes (Fig. 1a) can be seen in the other projections of Figure 3 and is denoted by T_+ or T_-. The magnitude of the talc stagger in projection is *b*/6 (note $b = a\sqrt{3}$). The component in (001) of the displacement between the No. 4 and No. 7 planes (Fig. 1a) defines the B-sheet shift vector. Therefore both the talc stagger and the B-sheet shift vector lie in (001). The offset across the B sheets is similarly denoted by B_O, B_+ and B_-. The B-sheet shift vectors are either of length *a*/3 parallel to any of the three a-axes shown in Figure 1 or of length *b*/3 perpendicular to any of the three a-axes. When viewed down ⟨100⟩, or ⟨110⟩, B-sheet shift vectors of length *a*/3 have a projected length of 0 or *b*/6. B-sheet shift vectors of length *b*/3 have projected lengths of *b*/6 or 2*b*/6 when viewed along these directions. The total offset, indicated by a solid line, is the projected displacement of a single chlorite unit. Thus, the chlorite shift vector can be denoted by the two individual layer offsets; for example, the notation for the chlorite shift vector of D^+ in Figure 3 is T_+B_0.

The repeat distance parallel to the layers in the projections of Figure 3 is *b*/2; therefore, a shift having projections 2*b*/6 is equivalent to one that has a projection of

Table 2. Summary of 1-Layer Polytypes (from Bailey and Brown, 1962)

Symbol	Space Group	Unique Angle	Equivalent Structure**	Enantiomorphic Structure***
Ia-1	Cm	β = 97°	Ib-2	-
Ia-2*	C2/m	β = 97°	-	-
Ia-3	C1	β = 97°	Ib-6	Ia-5
Ia-4	C$\bar{1}$	β = 97°	Ia-6	-
Ia-5	C1	β = 97°	Ib-4	Ia-3
Ia-6	C$\bar{1}$	β = 97°	Ia-4	-
Ib-1*	C2/m	β = 90°	-	-
Ib-2*	Cm	β = 97°	Ia-1	-
Ib-3*	C$\bar{1}$	α = 102°	Ib-5	-
Ib-4*	C1	β = 97°	Ia-5	Ib-6
Ib-5	C$\bar{1}$	α = 102°	Ib-3	-
Ib-6	C1	β = 97°	Ia-3	Ib-4
IIa-1*	C2/m	β = 97°	-	-
IIa-2*	Cm	β = 90°	IIb-1	-
IIa-3*	C$\bar{1}$	β = 97°	IIa-5	-
IIa-4*	C1	α = 102°	IIb-5	-
IIa-5	C$\bar{1}$	β = 97°	IIa-3	-
IIa-6	C1	α = 102°	IIb-3	IIa-4
IIb-1	Cm	β = 90°	IIa-2	-
IIb-2*	C2/m	β = 97°	-	-
IIb-3	C1	α = 102°	IIa-6	IIb-5
IIb-4*	C$\bar{1}$	β = 97°	IIb-6	-
IIb-5	C1	α = 102°	IIa-4	IIb-3
IIb-6	C$\bar{1}$	β = 97°	IIb-4	-

*Selected among 12 unique polytypes.

**After 180° rotation about Y axis.

***Only one member of an enantiomorphic pair is included in unique polytypes.

$-b/6$. Thus, projection E^- of Figure 3 is indistinguishable from F^+, and E^+ is indistinguishable from F^-. The other projections in Figure 3 are unique. Table 3 indicates which of the projections would be seen when viewing down the [100], [110], and [1$\bar{1}$0] axes.

Other important features of Figure 3 are the dashed circles situated between the T layers and B sheets. Computed images show that these circles correspond to areas of maximum intensity (white spots) in HRTEM images taken at optimum defocus (Fig. 5). These white spots are similar to those observed in HRTEM images of mica (Iijima and Buseck, 1978)[2] and are useful for distinguishing the chlorite polytype projections.

Figure 5 illustrates calculated HRTEM images of each of the five types of projections together with schematic drawings of the chlorite structure. Note that on HRTEM images it is possible to resolve relative shifts across T layers and B sheets, and thus to ascribe the proper T_+, T_0, T_- and B_+, B_0, B_- notations to each. The offset across the T layer may be unambiguously recognized since the length of the talc stagger can only be 0 or $\pm b/6$ in projection. However, there is multiplicity in the choice of offsets across the B sheet since it can have values of 0, $\pm b/6$ or $\pm b/3$ in projection. The equivalence of projections of $-b/6$ and $b/3$, as explained above, leads to the multiplicity in the choice of the projected B-sheet shift vector. Thus, we have adopted a convention to specify the projection of the offset across the B sheet (shown in Fig. 5 as the dashed vectors across the B sheet) as the vector that makes the smallest angle with **c*** (i.e., the normal to (001)). As a consequence of this convention, the projection F^+ is used instead of E^-, and similarly F^- is used rather than E^+ (Fig. 5). That is, a B-sheet vector of magnitude $+b/6$ would be chosen instead of the equivalent $-b/3$ shift and the shift $-b/6$ would be chosen instead of a $+b/3$ shift.

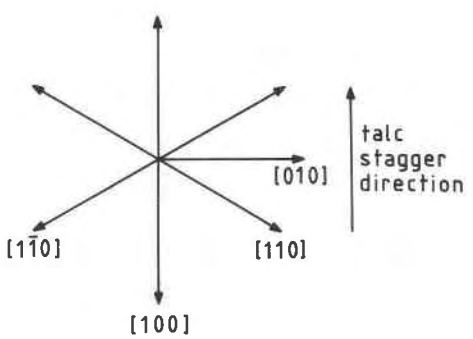

Fig. 2. Axial system for single-layer chlorite polytypes. [$\bar{1}$00] is defined as parallel to the talc-stagger direction. This axial system differs from that of Bailey and Brown (1962) and is used in this study for its convenience in describing the projections seen in electron micrographs.

Semi-random polytypes

The above discussion on chlorite polytypism has considered one-layer polytypes. Bailey and Brown (1962) reported that only three of the 12 possible regular stacking polytypes have been observed. X-ray diffraction patterns of 0*kl* nets commonly display streaking along **c*** for reflections of type $k \neq 3n$; such streaking indicates stacking disorder along **c**. Bailey and Brown showed that mixtures of polytypes related by $\pm b/3$ translations perpendicular to any of the three **a**-axes shown in Figure 1 are responsible for these effects. Sets of one-layer polytypes that are related by $b/3$ shifts constitute a semi-random stacking sequence as defined by Bailey and Brown. For example, polytypes Ib-1, Ib-3, and Ib-5 are related by $b/3$ shifts and form the Ib-odd semi-random stacking sequence. Similarly Ia-, IIa-, IIb-odd and Ia-, Ib-, IIa-, IIb-even each comprise a semi-random stacking sequence. In such semi-random stacking sequences individual polytype nomenclature loses its significance, and therefore a Ib designation now refers to either set of Ib-

[2] The white spots in the mica study of Iijima and Buseck (1978) were assumed to represent empty tunnels in the interlayer region. These tunnels alternate with occupied interlayer sites. However, calculations of a $2M_1$ biotite indicate that these areas of maximum intensity correspond to the interlayer cation positions. This change does not significantly affect the results of Iijima and Buseck (1978) since it involves a shift common to all layers.

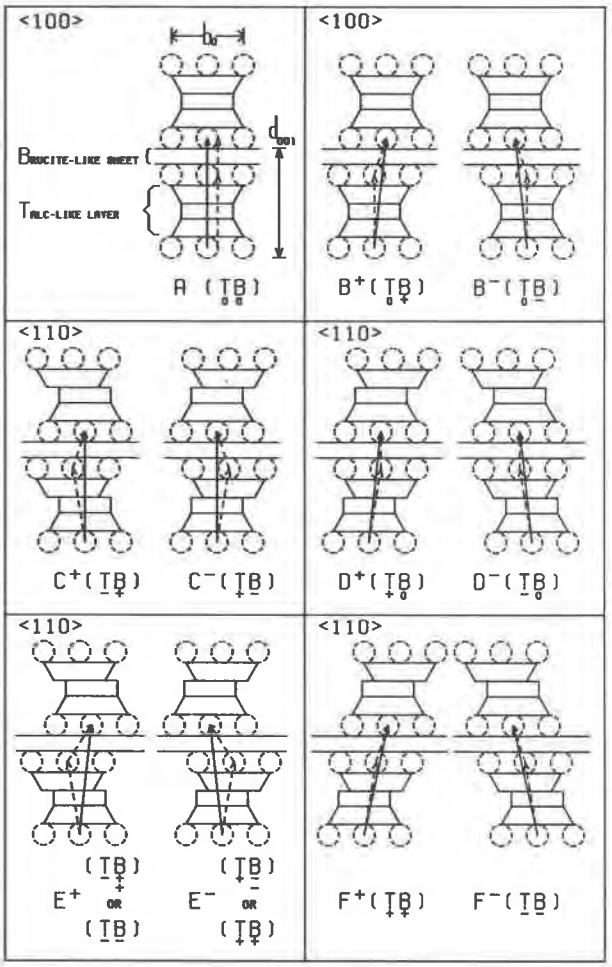

Fig. 3. Schematic diagrams of projections of one-layer chlorite polytypes viewed down ⟨100⟩ (A, B^+, B^-) and ⟨110⟩ (C^+, C^-, D^+, D^-, E^+, E^-, F^+, F^-). The dashed circles between the T layers and B sheets correspond to areas of maximum intensity on HRTEM images. The dashed vectors represent the component shifts across the T layers and B sheets, the sum of which equals the resultant chlorite shift vector, drawn as a solid line; in most cases this shift vector is the projection of the c-axis. The projection of the shift across the T layers is always $\pm b/6$, corresponding to $a/3$ absolute shifts. Since not all polytypes have identical orientation of axial systems, confusion in axis nomenclature is minimized by defining $[\bar{1}00]$ as parallel to the initial "T stagger," and the other directions are as indicated in Fig. 2. This convention is retained throughout the paper.

odd or Ib-even sequences. This leads to eight sets of semi-random polytypes, of which six are unique (Bailey and Brown, 1962). A crystal that has semi-random disorder will contain chlorite units from only one of these six unique groups. Table 4 is a list of these semi-random polytypes.

Results and discussion

X-ray precession analysis

X-ray precession photos indicate an ordered structure with a monoclinic unit cell, $\beta = 97°$, and mirror symmetry. Intensities of $h0l$ reflections indicate a IIb polytype. Since only one IIb polytype exists with $\beta = 97°$ and mirror symmetry, this polytype was uniquely determined among the 12 regular stacking sequences as IIb-2. This is the most abundant polytype found by Bailey and Brown (1962) in their extensive survey of natural chlorites.

Figure 6a is a zero level [110] precession photo of chlorite exposed for 60 hours. Very slight streaking parallel to c^* was observed along the $0kl$ rows with $k \neq 3n$ and indicates some stacking disorder. No evidence was present to suggest a multi-layer stacking sequence.

Electron diffraction and HRTEM

Figure 6b shows a typical electron diffraction pattern of chlorite taken from a region of a crystal several thousand ångströms in diameter. The zone axis, ⟨100⟩ or ⟨110⟩ (assuming $2/m$ symmetry), cannot be determined unam-

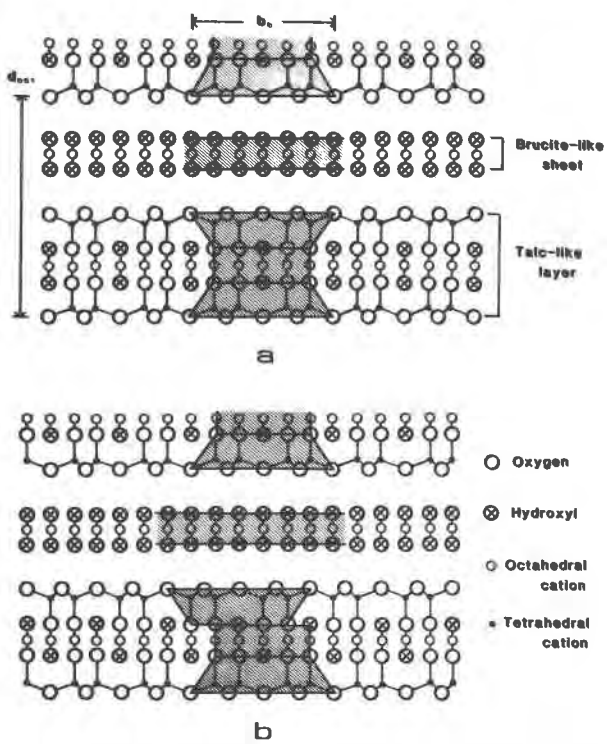

Fig. 4. Idealized schematic representation of the chlorite structure viewed parallel to the layers. The shaded segments denote that portion of the structure that makes up the I-beams used in Fig. 3. In (a), the talc stagger is parallel to the projection direction. In (b) the talc stagger-direction is not parallel to the projection, and therefore there is an offset within the I-beam. These figures respectively correspond to projections A and C^+ in Fig. 3.

Table 3. Projections of the one-layer chlorite polytypes (cf. Fig. 3) as seen sighting down [100], [110], and [1$\bar{1}$0] referred to the axes shown in Fig. 4.

One-layer Polytype		[100]	[110]	[1$\bar{1}$0]
Ia - 1		A	$E^-(F^+)$	$E^+(F^-)$
- 2		A	D^+	D^-
- 3		B^-	C^-	D^-
- 4		B^-	$E^-(F^+)$	C^+
- 5		B^+	D^+	C^+
- 6		B^+	C^-	$E^+(F^-)$
IIa - 1		A	D^+	D^-
- 2		A	C^-	C^+
- 3		B^-	$E^-(F^+)$	C^{-+}
- 4		B^-	D^+	$E^+(F^+)$
- 5		B^+	C^-	$E^+(F^-)$
- 6		B^+	$E^-(F^+)$	D^-
Ib - 1	IIb - 1	A	C^-	C^+
- 2	- 2	A	$E^-(F^+)$	$E^+(F^-)$
- 3	- 3	B^-	D^+	$E^+(F^-)$
- 4	- 4	B^-	C^-	D^-
- 5	- 5	B^+	$E^-(F^+)$	D^-
- 6	- 6	B^+	D^+	C^+

biguously because of the streaking of the $k \neq 3n$ reciprocal lattice rows. However, intensity maxima (arrowed) occur in these rows, corresponding to intensities expected for the ⟨110⟩ zones on a monoclinic-shaped unit cell with $\beta = 97°$. This fact, coupled with the observation that high-resolution micrographs of the crystal in this orientation yield offsets across the T layer (which do not occur when viewed down [100], see Fig. 3), has led to the indexing of Figure 6 to correspond to one of the ⟨110⟩ zone axes. The origin of the diffuse intensity in the 0*kl* reciprocal lattice rows where $k \neq 3n$ most likely arises from isolated stacking faults having translational or rotational randomness. The presence of strong streaking in the $k \neq 3n$ rows of selected-area electron diffraction patterns shows that, even though the X-ray diffraction patterns indicate an ordered structure, the crystal does contain highly disordered regions.

The 14.2Å periodicity of single-layer chlorite is apparent in the one-dimensional lattice fringe images that were recorded using only the 00*l* reflections (Fig. 7). A pair of bright- and dark-field images (Figs. 7a, b) were taken from the same region of the crystal. Such images are useful for finding irregular periodicities or the inclusion of extra T layers, B sheets, or other layers, such as partially dehydrated talc layers or brucite sheets, if they occur. However, we did not observe any irregularities in the (001) periodicities in any of the specimens that we examined; thus, the variations in image contrast in Figure 7 are caused by disorder in stacking sequences of the 14.2Å unit. The images potentially can also provide information on the occurrence of multi-unit polytypes, enantiomorphs, and twinning.

Image contrast such as in Figure 7 depends on specimen tilt and defocus of the microscope, and thus care must be used in the interpretation of such micrographs. The regions where the 14.2Å fringes appear in both images, indicated by "1," have a structure of ordered single-layer chlorite with widths of five or six unit cells parallel to c*. Dark-field images are more sensitive to low intensity scattering such as that from small regions of

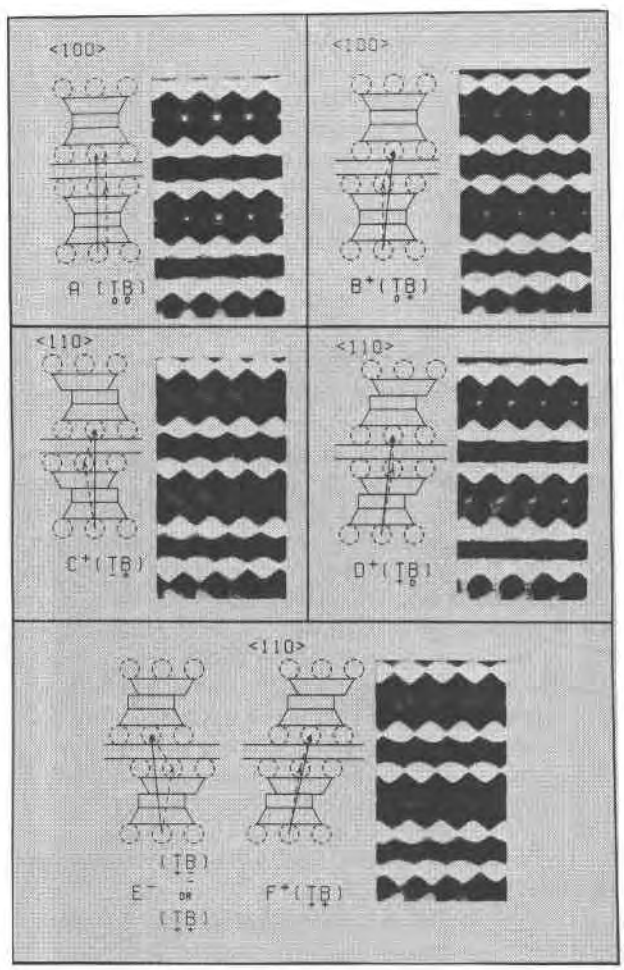

Fig. 5. Schematic diagrams of selected one-layer polytypes together with calculated HRTEM images. Areas of maximum intensity on the calculated images correspond to the dashed circles located between the T layers and B sheets. The vectors on the drawings have the same meaning as in Fig. 3. The images were computed at an underfocus of 1050Å for C_s = 2.2 mm, an accelerating voltage = 100kV, 2.4mrad divergence, and a 100Å spread in defocus. A beam-limiting aperture was not used. The crystal thickness is 16Å.

Table 4. Semi-random polytypes

Ia-even	= Ia, β = 97°
Ia-odd = Ib even	= Ib, β = 97°
IIa-even = IIb odd	= IIa, β = 90°
IIa-odd	= IIa, β = 97°
Ib-odd	= Ib, β = 90°
IIb-even	= IIb, β = 97°

multiple-layer polytypes or isolated stacking faults. Thus, Figure 7b shows greater contrast in the irregular regions of the crystal than does the bright-field image. Figure 7b shows narrow regions where apparent repeats of 28Å and 43Å seem to occur, corresponding in appearance to two-layer (14.2 × 2) and three-layer (14.2 × 3) chlorite polytypes; they are indicated by "2" and "3," respectively. However, as these are fringe images it is not possible to interpret these unambiguously as n-layer polytypes, since only 00*l* diffractions contribute to the image. In order to resolve this ambiguity, images containing information from beams other than the 00*l* row are needed.

HRTEM images and computation

A high-resolution image of a crystal in the same orientation as in Figure 6b is shown in Figure 8. One of the most prominent features of Figure 8, best observed by viewing at a low angle perpendicular to **c***, are dark fringes of regularly alternating width that are separated by rows of white spots. The wider fringes correspond to T layers and the narrower ones correspond to B sheets of the chlorite structure. The image shows that the T layers and B sheets alternate regularly without exception and that no additional types of layers occur, confirming the tentative interpretation of Figure 7. This lack of intercalation of other types is in contrast to the results illustrated in Veblen (1983), where mixed layering of extra brucite-like or talc-like layers within chlorite can be observed. In addition, fine scale intergrowths of isolated serpentine or extra talc-like layers within chlorite-type structures have been observed by Buseck et al. (1980) and Veblen and Buseck (1981).

As shown in Figure 5, the regions of high intensity in high-resolution images of chlorite can be used to determine the projected talc-stagger direction and the projected B-shift vector. Although the images in Figure 5 were computed for thin crystals at optimum (Scherzer) defocus for the JEOL 100B microscope, the correlation between the regions of high intensity and the chlorite shift vector holds over a wide range of defocus values and crystal thicknesses. A calculated through-focus series of images for the [110] zone of the IIb-2 polytype is shown in Figure 9. Images (at optimum defocus for the same zone and crystal) over a range of crystal thicknesses are shown in Figure 10. Figures 9 and 10 indicate the range of defocus and thickness for which regions of high intensity in HRTEM images may be used to find the shift vectors of chlorite crystals.

The measured widths of the T layers and B sheets in Figure 8 are not in agreement with the dimensions of approximately 9.26Å and 4.73Å respectively obtained from X-ray studies. In Figure 8 the apparent widths of the T layers are ~8.7Å and those of the B sheets are ~5.3Å. Similar anomalous values have been noted by Veblen (1983). Measurements of computed images of the chlorite IIb-2 polytype yield values of 8.6Å and 5.4Å for the thicknesses of the T layers and B sheets, respectively. These measurements are within experimental error of those obtained from the micrograph.

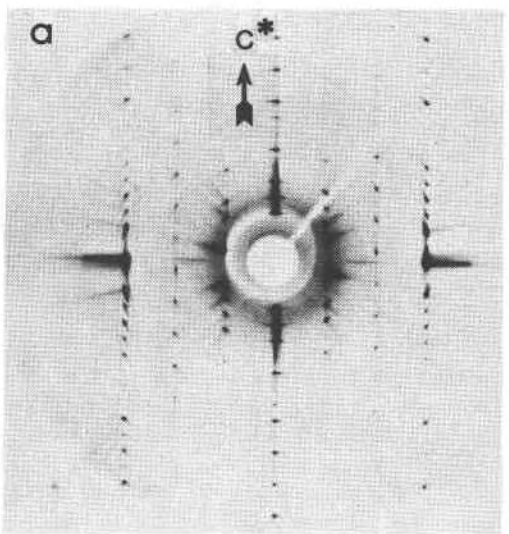

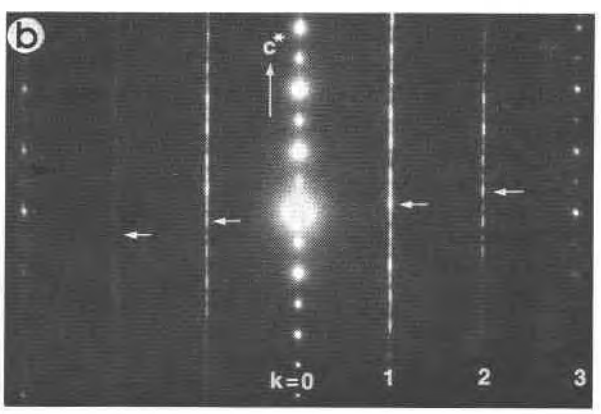

Fig. 6. (a) 0-level [110] precession photo of chlorite exposed to Zr-filtered Mo radiation for 60 hours. (b) Electron diffraction pattern of a fragment of chlorite crystal showing sharp spots in the $k = 0$ and $k = 3$ rows and pronounced streaks in the $k = 1$ and $k = 2$ rows. Weak maxima (arrowed) in the streaks indicate a monoclinic structure.

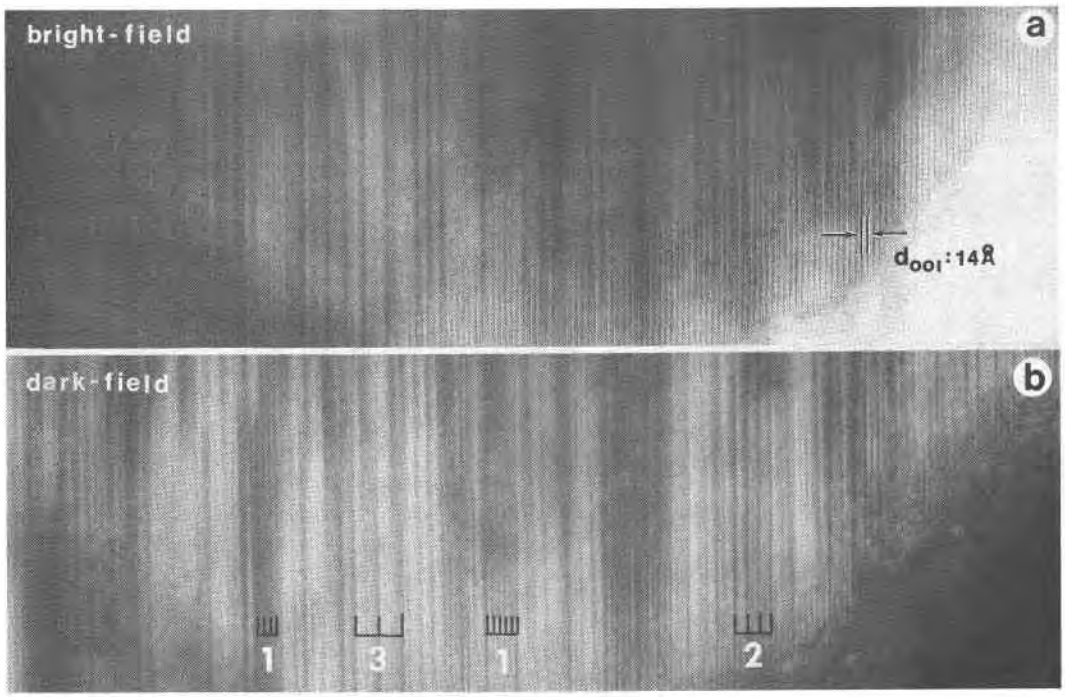

Fig. 7. A pair of electron micrographs comparing (a) bright-field and (b) dark-field images recorded from the same area of a crystal. The regions where the 14.2Å fringes appear in both images, indicated by "1," consist of an ordered single-layer chlorite. Regions having apparent repeats of 28Å and 43Å in the dark-field image, indicated by "2" and "3" respectively, should not be interpreted as polytypes because no such periodicities are evident in the bright-field image.

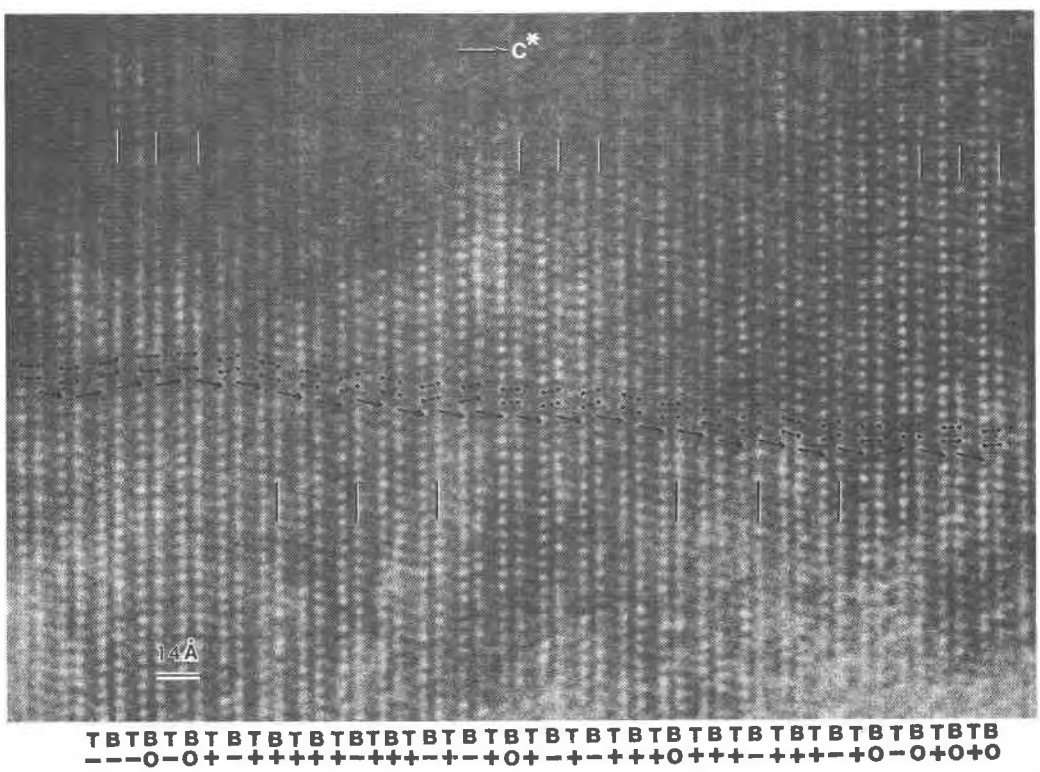

Fig. 8. A high-resolution image of chlorite showing the alternating talc-like layers (T) and brucite-like sheets (B) separated by rows of white spots. These spots correspond to the areas of dashed circles in Fig. 3. The arrows indicate the shifts across the T layers and the lines indicate the shifts across the B sheets. These markings correspond to the dashed vectors used in Fig. 5.

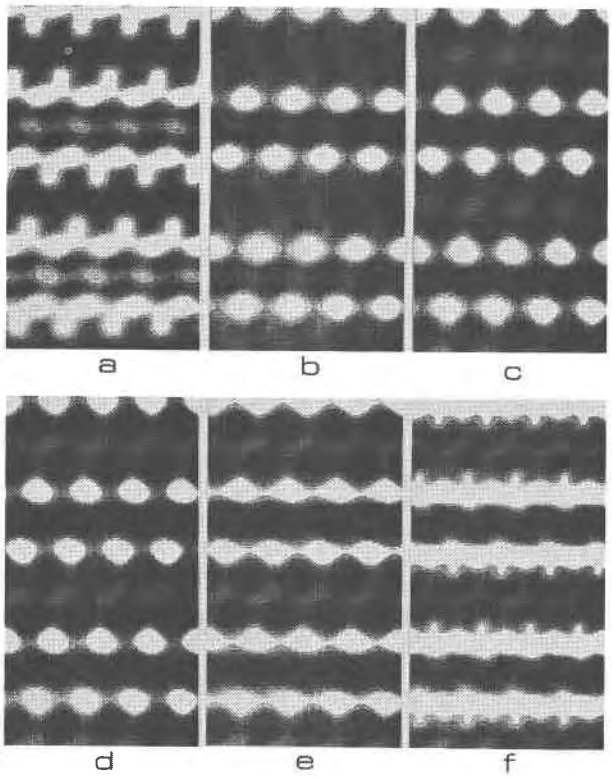

Fig. 9. Through-focus series of images computed for the [110] zone of the IIb-2 polytype. The defocus values are (a) −700Å, (b) −800Å, (c) −950Å, (d) −1050Å, (e) −1150Å and (f) −1250Å (all underfocus). Optimum defocus occurs at 1050Å underfocus (d). The crystal thickness in these images is 79.5Å. The other instrumental and specimen parameters are identical to those used for Fig. 5.

These deviations from the actual values of the real-space structure illustrate the pitfalls of trying to derive too much detail from high-resolution images. Figure 8 represents the basic structure of the chlorite, but problems may arise if high-resolution images are interpreted to represent an exact correspondence with projected charge density.

Similar differences between projected charge densities and structures have been reported in even simple structures such as Si (Hutchison et al., 1981) and SnO_2 (Smith et al., 1981). In order to obtain a true structure image the specimen must be thin, the number of diffracted beams contributing to the image must be large, and the beams must recombine in phase. Lens aberrations and beam divergence truncate the high-order beams and change the relative phases of the lower-order beams. By choosing a suitable defocus (around the Scherzer defocus), the relative phase changes introduced by lens aberrations can be minimized for the low-order beams. The truncation of higher order beams can be reduced only by changing instrumental parameters such as decreasing the spherical aberration coefficient (C_s). Thus, any HRTEM image overemphasizes the contribution of the lower-order beams to the image. This not only changes the relative intensities within the image, but also can change the spacing of image detail. The excellent agreement between the spacings in the computed images of Figure 5 and the HRTEM image of Figure 8 shows the usefulness and importance of image simulation for HRTEM (see also, O'Keefe et al., 1978; O'Keefe and Buseck, 1979).

Differences between the spacings of details within an image and the true spacings of the crystal structure are reduced as increasing numbers of beams contribute to the image. This is illustrated for chlorite in Figure 11a. In this computed image the crystallographic and instrumental parameters are identical to those used for Figures 9 and 10 except that the value of C_s has been reduced to 0.7 mm. The separations of bands of high intensity (arrowed) in the image shown in Figure 11a are in reasonable agreement with the widths of the talc-like layer and brucite-like sheets determined from X-ray measurements.

It is interesting that, since the regions of high intensity in the image do not correspond to any prominent structural feature, they would disappear if the number of beams contributing to the image was increased (for example, by using a microscope with a lower C_s). In decreasing the C_s

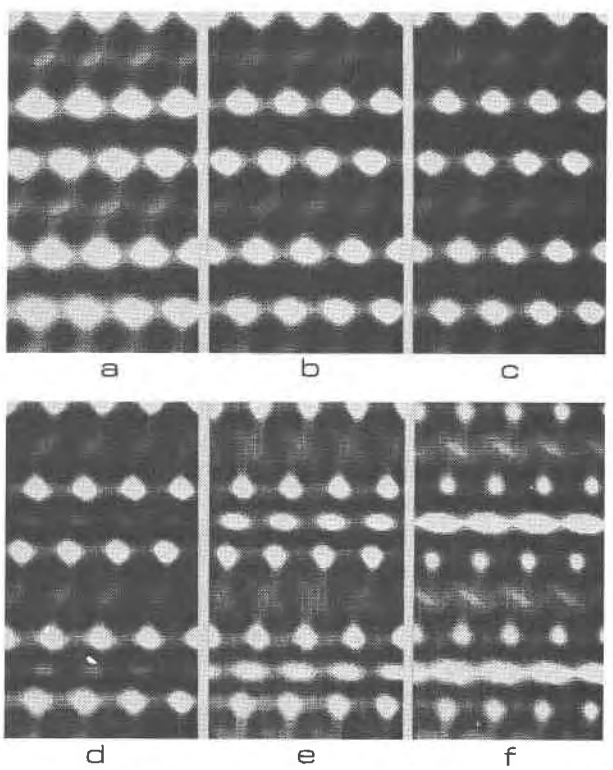

Fig. 10. Computed images as a function of crystal thickness for the [110] zone of the IIb-2 polytype. The thickness values are (a) 39.8Å, (b) 79.5Å, (c) 119.3Å, (d) 159.0Å, (e) 198.8Å and (f) 238.5Å. The other instrumental and specimen parameters are identical to those used for Fig. 5.

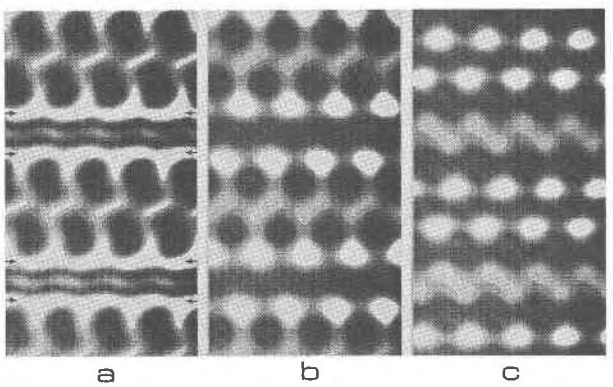

Fig. 11. Computed images for the [110] zone of a 79.5Å thick crystal of the IIb-2 polytype. All images are for C_s = 0.7 mm and an accelerating voltage of 100kV. Figures (a) and (b) are for optimum defocus (500Å underfocus) while (c) is for gaussian (0Å) focus. A beam-limiting aperture is not used in (a) and (c), while in (b) a circular aperture is centered on 000 and only includes reflections out to 210.

from 2.2 mm to 0.7 mm (Figs. 5 and 11a, respectively), the white spots have merged to form bands of high intensity (arrowed). The image in Figure 11a does not allow the simple interpretation that can be achieved from images such as those in Figures 5, 9, and 10. As the white spots in Figure 8 greatly facilitate the identification of the T- and B-shift vectors, it would be advantageous to decrease the resolution in a low C_s microscope by introducing an objective (beam limiting) aperture that would only include beams of the first order in k. A (computed) image in which a beam-limiting aperture has been introduced is shown in Figure 11b. This image is similar to those of Figures 5, 9, and 10 and, in Figure 11b the white spots (and therefore the projected shift vector) can be clearly seen.

Alternatively, the effective resolution of the microscope may be reduced by using a suitable value of defocus such as that shown in Figure 11c. The shifts parallel to c* of the areas of high intensity in these Figures result from the phase changes introduced by dynamical diffraction.

HRTEM *images: interpretation*

Figure 3 may be used as an aid for interpreting the high-resolution micrograph of Figure 8. As stated above, the areas of high intensity on the computed images (the white dots on the micrograph) are represented by dashed circles on the schematic diagrams of Figure 3. The positions of the dots can be used to determine the relative shifts across the layers, as seen in Figures 5 and 3. The projected shift vectors across the T layers and B sheets are determined unambiguously by recognizing that these shifts occur in increments of $b/6$.

It can be seen from Figure 3 that the interpretation of projected shift vectors from the high-resolution image is quite straightforward. Figure 8 may be interpreted by noting that a majority of the shifts across the T layers are T_+, whereas those across the B sheets vary among B_+, B_0, and B_- with no apparent pattern. This sequence can be explained in terms of semi-random stacking, where each chlorite layer is related by $b/3$ shifts in (001).

In Figure 8 the observed sequence of $T_+B_-T_+B_+T_+B_+T_+B_-T_+B_+T_+B_-T_+B_-T_+B_0T_+B_-T_+B_-T_+B_+T_+B_0T_+B_+T_+B_-T_+B_+T_+B_-T_+B_0$ indicates projections (Fig. 3) of C^-, F^+, F^+, C^-, F^+, C^-, C^-, D^+, C^-, C^-, F^+, D^+, F^+, C^-, F^+, C^-, D^+ respectively. As the majority of the sample is of the IIb-2 type, these projections can be interpreted as IIb-4,-2,-2,-4,-2,-4,-4,-6,-4,-4,-2,-6,-2,-4,-2,-4,-6, respectively, constituting a IIb-even semi-random stacking sequence.

From the HRTEM micrograph alone, it would be equally reasonable to interpret this sequence as resulting from any of the semi-random stacking sequences. However, as shown above, the electron diffraction pattern (Fig. 6b) displays intensity maxima in the $k \neq 3n$ reciprocal lattice rows that correspond to a structure with $\beta = 97°$. Thus, the IIb-odd and Ib-odd semi-random sequences that have $\beta = 90°$ must be eliminated (Table 4). Furthermore, X-ray data show that a majority of the crystal is of the IIb-2 type and confirm the interpretation of the sequence of shifts given above. Using HRTEM imaging alone, an unambiguous determination of stacking sequences requires imaging more than one [uv0] zone of the same area of crystal.

The talc staggers in semi-random stacking sequences must all have the same signs. However, on the extreme right side of Figure 8 there is an isolated T_-, and this indicates a rotational fault of $-120°$ or 180°. The left side of the image also illustrates a small area with T_-, resulting from the same rotation. The tetrahedral sheets of the T layers suffer similar ditrigonal distortion to that of Li-free mica (Shirozu and Bailey, 1965), and therefore 180° layer rotations probably do not occur for reasons analogous to those presented by Ross et al. (1966). Thus, the rotation is probably $-120°$.

Chlorite suffers relatively rapid radiation damage in the electron beam. Figure 12 shows an early stage of decomposition of chlorite, in which several individual T layers have been decomposed preferentially, relative to the B sheets. However, extended exposure to the beam also causes B sheet destruction. The decomposed areas appear to become amorphous, but B sheets at both sides of the decomposed T layers remain undamaged. Veblen and Buseck (1981), in a study of biopyriboles, have also found that talc is unstable in the electron beam, in that case when surrounded by double- or triple-chain pyriboles.

Brindley and Ali (1950) studied the dehydration of penninite chlorite by heating; they reported that at about 600°C the B sheet was greatly modified whereas the T layer remained unchanged, in contrast to our results. These results suggest that radiation damage to chlorite is

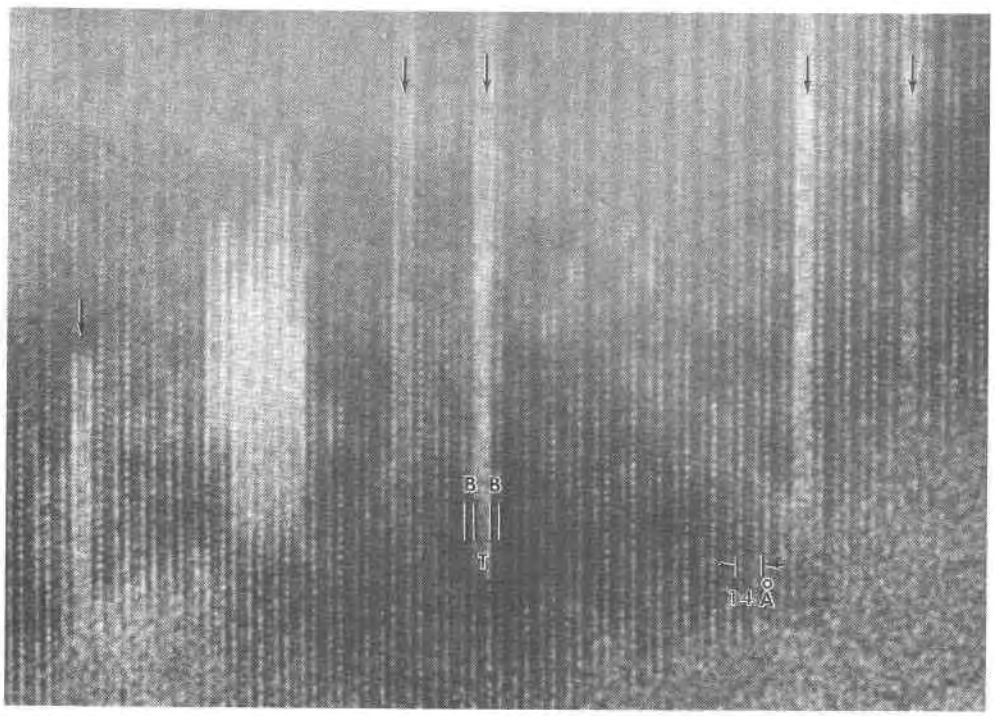

Fig. 12. High-resolution structure image of a crystal showing the effect of electron beam irradiation in the electron microscope. Some of the T layers (arrowed) have been damaged selectively and have become amorphous. The damage is confined to individual T layers.

not a pure dehydration process induced by electron beam heating.

Summary and conclusions

HRTEM methods and single-crystal X-ray precession methods were employed to investigate the details of chlorite polytypism. The HRTEM analysis yields information about stacking sequences on a unit cell level. It is possible to observe projected shift vectors across the T layers and B sheets in the chlorite structure, thereby distinguishing several different possible polytypes. However, unambiguous specification of polytypes is not possible from a single HRTEM image. In order to completely specify a polytype or semi-random stacking sequence, HRTEM must be combined with X-ray diffraction analysis or more than one zone of the same area of crystal must be imaged by HRTEM.

Interpretation of HRTEM images of chlorite was accomplished by using calculated HRTEM images. Five sets of unique projections result from viewing the 24 theoretical one-layer polytypes down their ⟨100⟩ or ⟨110⟩ zone axes based on a monoclinic cell with [$\bar{1}$00] parallel to the talc-stagger direction.

In the specific case of West Chester, Pennsylvania, clinochlore, single-crystal X-ray precession analysis indicates an ordered one-layer polytype of the IIb-2 type. Selected-area electron diffraction patterns from small regions of the crystal show diffuse scattering parallel to c* in 0kl rows with $k \neq 3n$, indicating shifts of magnitude $b/3$ between the chlorite layers.

HRTEM imaging shows that the T layers and B sheets alternate regularly in this crystal. (That is, stacking sequences in which a T layer or B sheet are missing were not observed.) The type of disorder observed in the crystal was predominantly semi-random stacking sequences with an occasional layer rotation.

Acknowledgments

Revisions of the original manuscript recommended by reviewers and D. R. Veblen are gratefully appreciated. This research was supported by NSF grant EAR-7926375 from the Earth Sciences Division of the National Science Foundation. Microscopy was performed in the Arizona State University Facility for High Resolution Electron Microscopy, which was established with support from the NSF Regional Instrumentation Facilities Program, grant CHE7916098.

References

Bailey, S. W. (1980) Summary of recommendations of AIPEA nomenclature committee on clay minerals. American Mineralogist, 65, 1–7.

Bailey, S. W. and Brown, B. E.[3] (1962) Chlorite polytypism: I.

[3] The order of the authors was reversed in this article as published; S. W. Bailey is the senior author (S. W. Bailey, pers. comm., 1982).

Regular and semi-random one-layer structures. American Mineralogist, 47, 819–850.

Brindley, G. W. and Ali, S. Z. (1950) X-ray study of thermal transformations in some magnesian chlorite minerals. Acta Crystallographica, 3, 25–30.

Buseck, P. R., Nord, G. L., Jr., and Veblen, D. R. (1980) Subsolidus phenomena in pyroxenes. In Pyroxenes, C. T. Prewitt Ed., Mineralogical Society of America Reviews in Mineralogy, 7, 117–211.

Hutchison, J. L., Anstis, G. R., Humphreys, C. J. and Ourmazd, A. (1981), Atomic images of silicon and related materials: fact or artefact? EMAG 1981, Institute of Physics Conference Series No. 61, 357–360.

Iijima, Sumio and Buseck, P. R. (1977) Stacking order and disorder in chlorite and mica. (abstr.) Transactions of the American Geophysical Union, 58, 524–525.

Iijima, Sumio and Buseck, P. R. (1978) Experimental study of disordered mica structures by high-resolution electron microscopy. Acta Crystallographica, A34, 709–719.

O'Keefe, M. A., Buseck, P. R. and Iijima, Sumio (1978) Computed crystal structure images for high resolution electron microscopy. Nature, 274, 322–324.

O'Keefe, M. A., Buseck, P. R. (1979) Computation of high-resolution TEM images of minerals. Transactions of the American Crystallographic Association, 15, 27–46.

Ross, Malcolm, Takeda, Hiroshi, and Wones, D. R. (1966) Mica polytypes: Systematic description and identification. Science, 151, 191–193.

Shirozu, Haruo and Bailey, S. W. (1965) Chlorite polytypism: III. Crystal structure of orthohexagonal iron chlorite. American Mineralogist, 50, 868–885.

Smith, D. J., Camps, R. A. and Freeman, L. A. (1981) Atomic resolution in the high voltage electron microscope. EMAG 1981, Institute of Physics Conference Series No. 61, 381–386.

Veblen, D. R. and Buseck, P. R. (1981) Hydrous pyriboles and sheet silicates in pyroxenes and uralites: Intergrowth microstructures and reaction mechanisms. American Mineralogist, 66, 1107–1134.

Veblen, D. R. (1983) Microstructures and mixed layering in intergrown wonesite, chlorite, talc, biotite and kaolinite. American Mineralogist, 68, 566–580.

Manuscript received, March 2, 1983;
accepted for publication, October 24, 1983.